PAPER • **OPEN ACCESS**

Cation exchange mediated synthesis of bright Au@ZnTe core–shell nanocrystals

To cite this article: Sadra Sadeghi *et al* 2021 *Nanotechnology* **32** 025603

OPEN ACCESS
IOP Publishing
Nanotechnology

Nanotechnology **32** (2020) 025603 (9pp)
https://doi.org/10.1088/1361-6528/abbb02

Cation exchange mediated synthesis of bright Au@ZnTe core–shell nanocrystals

Sadra Sadeghi[1], **Rustamzhon Melikov**[2], **Mehmet Sahin**[3] **and Sedat Nizamoglu**[1,2]

[1] Graduate School of Materials Science and Engineering, Koç University, Istanbul 34450, Turkey
[2] Department of Electrical and Electronics Engineering, Koç University, Istanbul 34450, Turkey
[3] Department of Materials Science and Nanotechnology Engineering, Abdullah Gul University, Kayseri 38080, Turkey

E-mail: snizamoglu@ku.edu.tr

Received 24 July 2020, revised 4 September 2020
Accepted for publication 23 September 2020
Published 14 October 2020

Abstract

The synthesis of heterostructured core–shell nanocrystals has attracted significant attention due to their wide range of applications in energy, medicine and environment. To further extend the possible nanostructures, non-epitaxial growth is introduced to form heterostructures with large lattice mismatches, which cannot be achieved by classical epitaxial growth techniques. Here, we report the synthetic procedure of Au@ZnTe core–shell nanostructures by cation exchange reaction for the first time. For that, bimetallic Au@Ag heterostructures were synthesized by using PDDA as stabilizer and shape-controller. Then, by addition of Te and Zn precursors in a step-wise reaction, the zinc and silver cation exchange was performed and Au@ZnTe nanocrystals were obtained. Structural and optical characterization confirmed the formation of the Au@ZnTe nanocrystals. The optimization of the synthesis led to the bright nanocrystals with a photoluminescence quantum yield up to 27%. The non-toxic, versatile synthetic route, and bright emission of the synthesized Au@ZnTe nanocrystals offer significant potential for future bio-imaging and optoelectronic applications.

Keywords: non-epitaxial, photoluminescence quantum yield, Au@ZnTe, core–shell, nanocrystals

(Some figures may appear in colour only in the online journal)

1. Introduction

The synthesis of core–shell nanocrystals has attracted significant attention due to the high versatility in the broad spectrum of chemical, optical and biological applications [1–5]. The core–shell nanocrystals often show a wide variety of optical and structural properties than the core material, which make them attractive for various applications. The shell can alter the properties of the core such as size mono-dispersivity, solubility, emission, stability and introduce novel electronic, magnetic, optical, catalytic, and chemical properties. Although significant achievements have been made towards the size control, composition, shape, and crystallinity of the core nanomaterials during numeric synthetic procedures [6, 7], the synthesis of the core–shell structures with unconventional optical and structural properties is still challenging due to the limitations associated with the precise control of the structure such as self-nucleation of the shell component and non-homogenous growth [8].

To realize such unusual nanostructures, non-epitaxial growth (cation exchange) uniquely offers the ability to grow

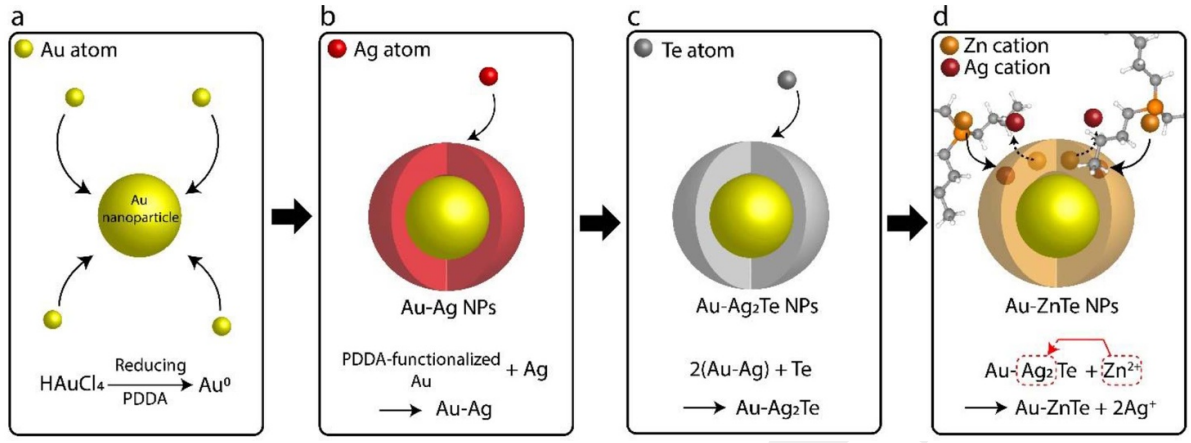

Figure 1. **(a)** The gold nanoparticles were synthesized by reducing $HAuCl_4$. **(b)** After the formation of the gold nanoparticles, the silver shell was formed by introducing $AgNO_3$. **(c)** By addition of the tellurium, silver telluride was formed as the shell for gold nanoparticles. **(d)** After the complete formation of the silver telluride shell, zinc cations and TBP were added to the reaction. The cation exchange between zinc and silver cations resulted in zinc telluride formation as the shell for gold nanoparticles.

heterostructures with large lattice mismatches. In the cation exchange reactions, only the precursor, which constitutes the shell cations are introduced to the reaction and the gradual replacement of the core cations with the introduced shell cations take place [9, 10]. In this approach, because the growth of the shell is fully governed by the chemical reactions inside the matrix, the crystal structure of the shell material will be independent of the core material [11]. The independency of the growth mechanism to lattice constraints in cation exchange reactions opens up a unique opportunity to synthesize wide spectrum of core–shell heterostructures with different crystal structures and large lattice mismatches such as Au-CdSe, Au-CdTe, Au-PbS, Au-ZnS, and Pt-CdS [12]. At the same time, the cation exchange reactions have been used for the synthesis of core–shell nanomaterials with small lattice mismatches such as PbSe-CdSe [13], PbS-CdS [14], and CuInS-ZnS [15] as well.

Herein, we report Au@ZnTe core–shell nanostructures by non-epitaxial growth for the first time. The synthesis procedure is based on the sequential replacement of Te and Zn ions on gold core nanoparticles that finally end-up with a highly-crystalline ZnTe shell. The structure of the nanocrystals are confirmed with XRD, TEM, HRTEM and EDS elemental mapping measurements that are supported by optical characterizations. The optimization of the synthesis led to the demonstration of efficient nanocrystals with a photoluminescence quantum yield (PLQY) of 27%.

2. Results

The lattice mismatch between core and shell material that have different crystallographic facets with curved surfaces affects the nucleation and growth strategy [16]. The large lattice mismatch (approximately $\sim 50\%$) between the gold (face-centered cubic structure with the lattice parameter of 4.065 Å) [17] and zinc telluride (zinc blende cubic structure with the lattice parameter of 6.101 Å) [18] prevents the possibility of epitaxial growth [12]. If the epitaxial growth would be performed, the unintentional crystalline imperfections such as poly-crystallinity, dislocations and strain-induced defects will lead to the core and shell segregation and the degradation of the optical and structural properties, especially in the thick shell formation [19, 20].

To synthesize Au@ZnTe nanocrystals, we employed a stepwise organometallic synthetic route, in which zinc telluride as the shell material was non-epitaxially grown onto the gold as the core material. In this method, the shell growth is fully governed by the thermodynamics of the reaction procedure within the matrix, and the formation of the ZnTe shell is not dependent on the crystallographic planes of the Au core material. Hence, the large lattice mismatch between the core and shell material will not be an obstacle for the formation of core–shell structure. The different steps of the synthesis are illustrated in figure 1. Firstly, the gold nanoparticles were synthesized by the reduction of Au^{3+} cations by reacting gold (III) chloride hydrate ($HAuCl_4$) and polydiallyldimethylammonium chloride (PDDA), which acts both as the reducing and stabilizing agent (figure 1(a)) [8]. Then, a metal with the soft Lewis acidity (e.g. silver) was grown on top of the gold core nanoparticles. Silver metal was selected as the outer shell material at this stage due to the high acid softness (acid softness $= +3.99$) [12] of silver cations, which enables to easily share electrons with the other soft bases and forms different types of complexes. Moreover, silver can easily be grown on various types of core nanoparticles with precise control of shell thickness [12]. In this step, the silver cations (Ag^{+}) was provided by reacting silver nitrate ($AgNO_3$) with the core gold nanoparticles (figure 1(b)). After the formation of Au@Ag nanoparticles, tellurium was added to the reaction to react with the silver and form silver telluride (Ag_2Te) as the shell compound due to $+2$ oxidation state of tellurium (figure 1(c)). Upon completion of the reaction, the color of the solution became darker, which indicated the formation of the Ag_2Te. In the next step, zinc cations (Zn^{2+}) were added to the reaction to perform the cation exchange between the zinc and silver cations. For

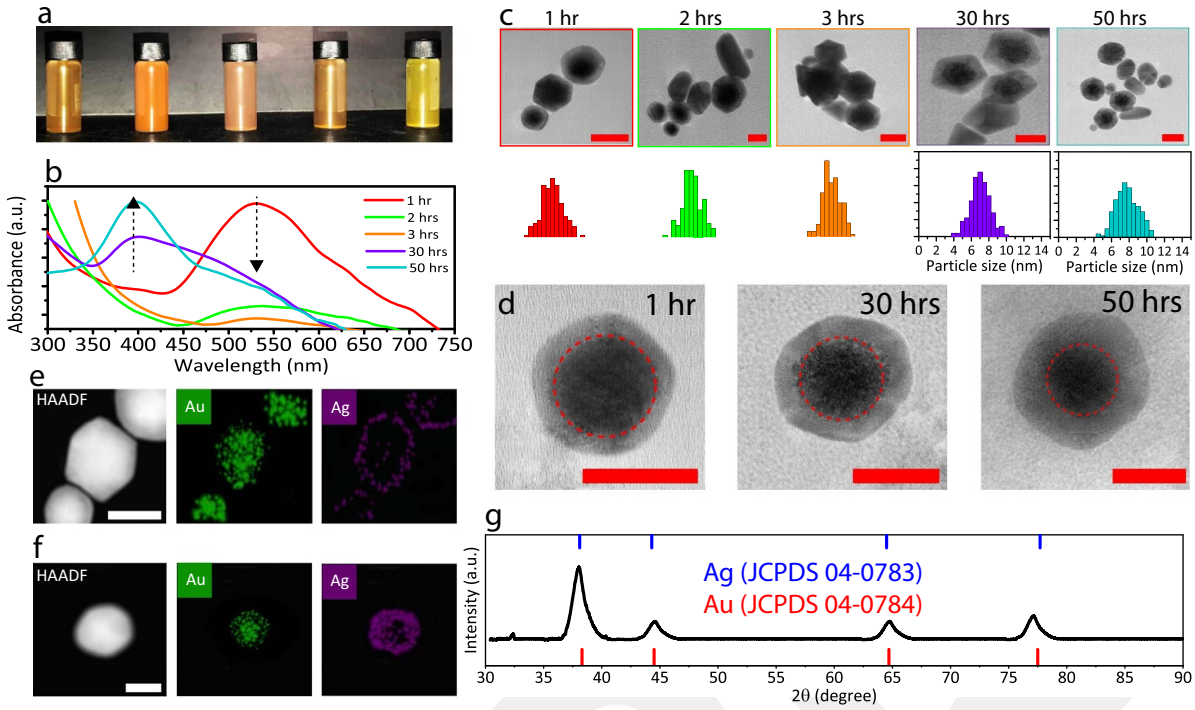

Figure 2. **(a)** The photograph of synthesized Au@Ag nanoparticles with different reaction times of (from left to right) 1, 2, 3, 30, and 50 h under ambient light. **(b)** The absorbance profile of the synthesized nanoparticles with different reaction times. By increasing the reaction time, the absorbance intensity of the gold decreases and the absorbance intensity of the silver increases due to the formation and growth of silver shell component. **(c)** The TEM image and size distribution of the synthesized Au@Ag nanoparticles at different reaction times of 1, 2, 3, 30, and 50 h. The size distribution was calculated from 200 particles in each image. **(d)** The TEM images of the spherical Au@Ag nanoparticles at different reaction times of 1, 30, and 50 h. The central dark areas represent the Au core nanoparticles and the bright surrounding regions correspond to Ag shell. HAADF-STEM images and EDS maps of Au and Ag from the synthesized Au@Ag core–shell nanoparticles at different reaction times of **(e)** 1 h, and **(f)** 50 h. **(g)** The XRD pattern of the synthesized Au@Ag core–shell nanoparticles with the reaction time of 50 h. The vertical red and blue lines represent the standard XRD peaks of Au and Ag. The scale bar is 5 nm in all TEM and HAADF-STEM images.

that, tributylphosphine (TBP) was selected due its soft base characteristics ($\beta > 6$) and acting as the phase transfer agent. The presence of large and relatively polarizable phosphorous (P) atoms in the chemical structure facilitates the bonding between zinc cations and TBP molecules. Based on the Lewis theory of hard soft acid base (HSAB), the soft acids tend to bind with the soft bases [21]. Hence, the TBP molecules bound with the free zinc cations in the reaction will replace the silver cations and form zinc telluride (figure 1(d)). The high acid softness of Ag^{+} favors the exchange process between Ag^{+} in the amorphous matrix (Ag_2Te) and Zn^{2+} in solution as long as the procedure is thermodynamically satisfied ($\Delta G > 0$).

To achieve the high photoluminescence quantum yield (PLQY) in the synthesized Au@ZnTe core–shell nanocrystals, the optical properties of the nanocrystals at different steps of the synthesis procedure need to be investigated and optimized. After the formation of the Au nanoparticles, the Ag shell was grown on top of the PDDA-functionalized Au nanoparticles. The absorbance profiles of the synthesized Au@Ag nanoparticles were recorded at different reaction times of 1, 2, 3, 30, and 50 h, respectively (figure 2(b)). At the initial reaction times of 1, 2, and 3 h, the absorbance profile showed a peak with higher intensity at ~535 nm, which corresponded to Au nanoparticles. By increasing the reaction time up to 30 and 50 h, the absorbance profile showed a shifted absorbance peak at ~401 nm due to Ag shell formation (figure 2(b)). By growing the shell thickness to 0.95 nm, the absorbance of the core–shell nanoparticles are dominated by the shell, which is similar to the previous studies [8, 22]. The photograph of the solutions with different reaction times under the ambient light also confirmed the different absorbance profiles due to the growth of the Au nanoparticles and the Ag shell formation (figure 2(a)).

In order to structurally analyze the Au@Ag nanoparticles, the transmission electron microscopy (TEM) images of them were recorded for different reaction times ranging from 1 h to 50 h (figures 2(c) and (d)). In the obtained TEM images, the central dark area corresponded to Au core region, whereas the surrounding brighter regions confirmed the Ag shell formation. At the same time, the size distribution of the synthesized Au@Ag nanoparticles were calculated (figure 2(c)). While the reaction time increases from 1 h to 50 h, the size of the Au core remained constant as 4.8 nm and the size of the Au@Ag nanoparticles increased from 5.6 ± 1.2 nm to 7.4 ± 1.2 nm due to the growth of the Ag shell, respectively (table 1). By considering the lattice parameter of the Ag crystal structure as 0.409 nm [23], the thickness of the Ag shell were grown from 1.0 to 3.2 monolayers.

The rather wide size-distribution of the synthesized Au@Ag nanoparticles specifically at higher reaction times of 30 and 50 h is attributed to the non-uniform growth of the

Table 1. The size and elemental analysis of the synthesized Au@Ag nanoparticles at different reaction times.

Reaction time (hrs)	Average Au@Ag particle size	Au core diameter	Ag shell thickness	Ag shell number of monolayers	Au (wt %)	Ag (wt %)
1	5.6 ± 1.2 nm	4.8 nm	0.4 nm	∼1.0 ML	73.27%	26.73%
2	5.8 ± 1.1 nm	4.8 nm	0.5 nm	∼1.2 ML	66.62%	33.38%
3	5.9 ± 0.9 nm	4.8 nm	0.55 nm	∼1.3 ML	58.81%	41.19%
30	6.7 ± 1 nm	4.8 nm	0.95 nm	∼2.3 ML	36.75%	63.25%
50	7.4 ± 1.2 nm	4.8 nm	1.3 nm	∼3.2 ML	29.27%	70.73%

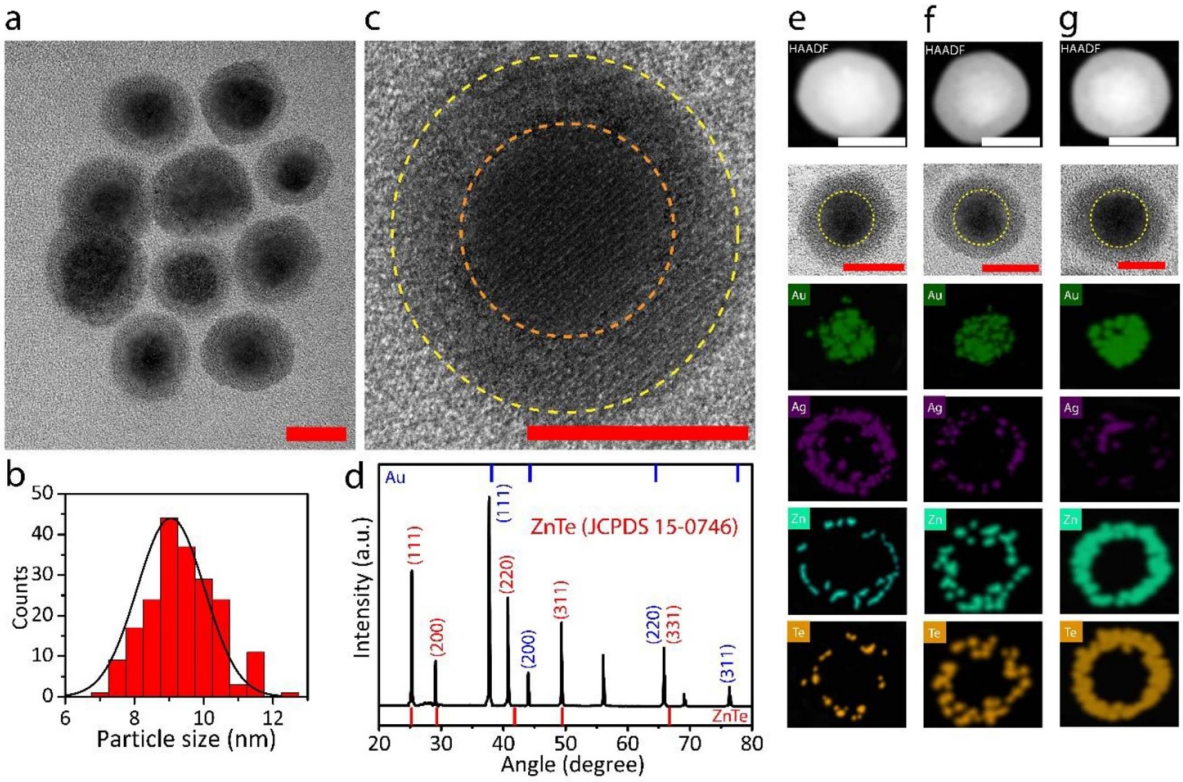

Figure 3. **(a)** The TEM image of the synthesized Au@ZnTe nanocrystals at the reaction time of 120 min from Au@Ag nanoparticles synthesized at 50 h. **(b)** The size distribution of the nanocrystals, which is calculated from 200 particles. **(c)** The HRTEM image of the synthesized Au@ZnTe nanocrystals at the reaction time of 120 min from Au@Ag nanoparticles synthesized at 50 h. The dashed orange and yellow lines represent the dark Au core and bright ZnTe shell regions. **(d)** The XRD pattern of the Au@ZnTe nanocrystals. The blue and red lines represent the standard XRD diffraction peaks of Au and ZnTe nanocrystals. HAADF-STEM images, TEM images, and EDS maps of Au, Ag, Zn, and Te from the synthesized Au@ZnTe core–shell nanocrystals at different cation exchange reaction times of **(e)** 1 min, **(f)** 20 min, and **(g)** 120 min. The scale bar is 5 nm in all TEM and HAADF-STEM images.

Ag shell on top of the gold core nanoparticles due to the simultaneous reduction of gold and silver sources in the ethylene glycol solution. The non-uniform growth of the Ag shell also led to the formation of non-spherical particles such as nanorods [24], which is observed in figure 2(c). The formation of the core–shell structure in the synthesized Au@Ag nanoparticles and the effect of the reaction time on the growth of the Ag shell were also investigated by performing the high-angle annular dark-field scanning transmission electron microscopy (HAADF-STEM) images together with the energy dispersive spectroscopy (EDS) elemental mapping (figures 2(e) and (f)). The recorded EDS maps clearly showed the presence of Au and Ag in the core and surrounding shell regions, respectively (figure 2(e)). At the same time, by increasing the reaction time from 1 h to 50 h, the growth of the Ag shell resulted in the higher concentration of the Ag in the shell region as expected (figure 2(f)). Moreover, the XRD pattern showed the face-centered cubic (FCC) structures of Au and Ag with similar diffraction peaks at 38.1°, 44.6°, 64.7° and 77.4°, which confirmed the presence of Au@Ag core–shell structure (figure 2(g)).

Once the Au@ZnTe nanocrystals were synthesized, their structural properties were investigated to confirm the formation of ZnTe shell on top of the Au nanoparticles. For that, TEM and high-resolution TEM (HRTEM) images of the synthesized nanocrystals were recorded (figures 3(a) and (c)). In the TEM images of the Au@ZnTe nanocrystals that were cation-exchanged for 120 min from the 50-hours-reacted Au@Ag nanoparticles, there is a clear differentiation between the dark Au core and bright ZnTe shell (figure 3(a)). The size

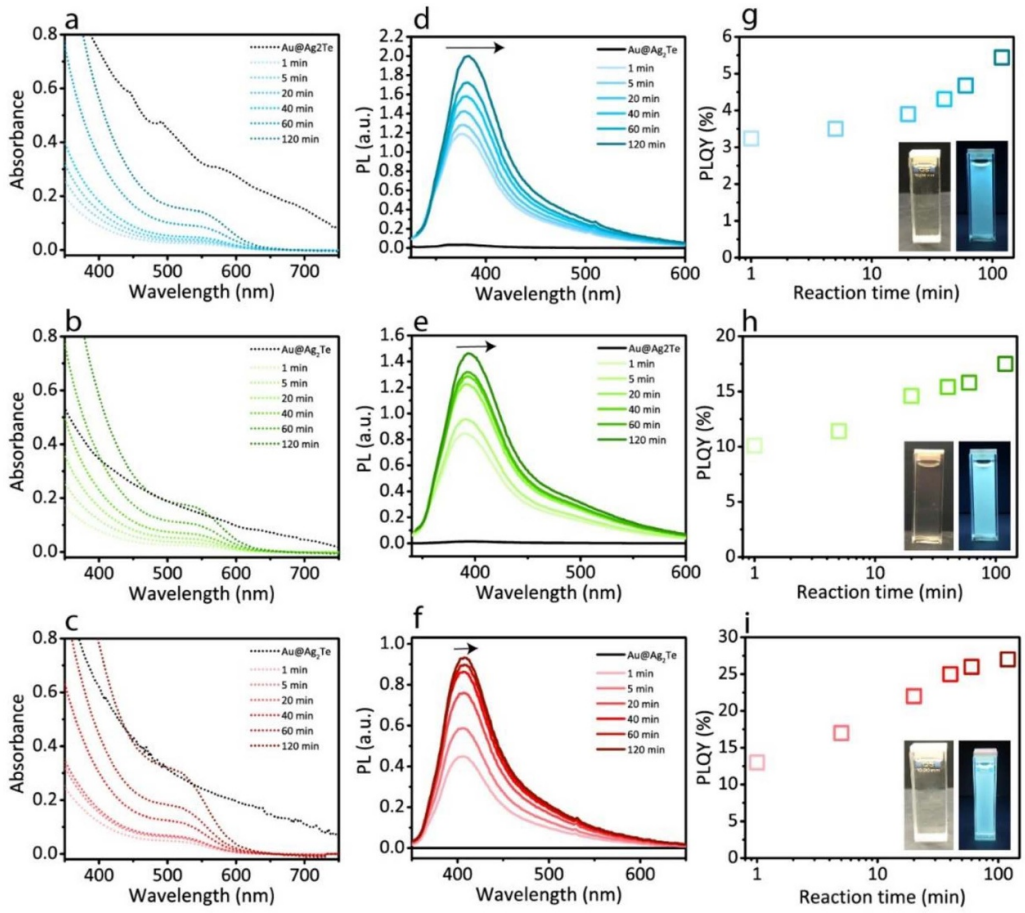

Figure 4. **((a), (d), (g))** The absorbance, normalized photoluminescence and PLQY of the synthesized Au@ZnTe nanocrystals with different reaction times ranging from 1 to 120 min from Au@Ag with the reaction time of 1 h. **((b), (e), (h))** The absorbance, normalized photoluminescence and PLQY of the synthesized Au@ZnTe nanocrystals with different reaction times ranging from 1 to 120 min from Au@Ag with the reaction time of 30 h. **((c), (f), (i))** The absorbance, normalized photoluminescence and PLQY of the synthesized Au@ZnTe nanocrystals with different reaction times ranging from 1 to 120 min from Au@Ag with the reaction time of 50 h. The insets in (g)–(i) are the photographs of the synthesized Au@ZnTe under ambient and UV illumination.

distribution analysis of the nanocrystals showed a change in the average size of the Au@Ag nanoparticles from 7.4 nm to 9.2 $\pm$ 0.95 nm due to the formation of the Ag_2Te interfacial layer before the cation exchange reaction (figure 3(b)). At the same time in HRTEM image (figure 3(c)), different lattice fringes are observable in both core and shell components, indicating highly-crystalline core–shell heterostructure. The XRD graph taken from Au@ZnTe nanocrystals also confirmed the presence of cubic Au and ZnTe crystal structures, in which the diffraction peaks at 25.2°, 29.1°, 40.8°, 49.4°, and 65.8° were compatible with the standard XRD diffraction peaks of ZnTe (figure 3(d)). We also performed HAADF-STEM images together with the EDS elemental mapping on the synthesized Au@ZnTe nanocrystals at the reaction times of 1, 20, and 120 min in order to confirm the presence of ZnTe shell (figures 3(e)–(g)). In the recorded EDS mapping images, the presence of Au is observed in the core, whereas Ag, Zn, and Te were mostly observed in the shell component. By increasing the reaction time from 1 min to 120 min, the Ag to Zn cation exchange reaction led to the higher concentration of Zn and Te in the surrounding shell region in comparison with Ag (figures 3(e)–(g)). At the reaction time of 120 min, almost a complete shell of ZnTe is formed around the Au core nanoparticles (figure 3(g)).

In order to investigate the effect of reaction time on the optical properties of the synthesized Au@ZnTe nanocrystals and enhancement of the PLQY, three different Au@Ag nanoparticles with different reaction times of 1, 30, and 50 h were selected for the cation exchange reaction. Then, Ag_2Te layer was formed on the Au core nanoparticles by addition of tellurium. The cation exchange reaction was performed up to 120 min and aliquots were taken at different time intervals. The absorbance, photoluminescence, and PLQY of the synthesized Au@ZnTe nanocrystals at different reaction times were shown in figure 4. The absorbance profile of the Au@ZnTe nanocrystals achieved from the Au@Ag nanoparticles at the reaction time of 1 h showed a distinctive absorption shoulder located at ~555 nm (figure 4(a)). This absorption shoulder corresponded to the 2.23 eV, which is compatible with the energy band gap of ZnTe semiconductor [25]. The presence of absorption shoulder similar to ZnTe band gap also confirmed the formation of the ZnTe

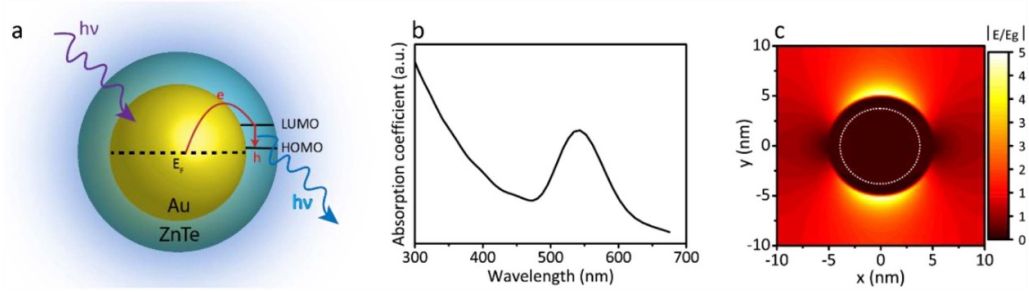

Figure 5. **(a)** The schematic showing the hot-electron injection in Au@ZnTe nanocrystals that can lead to photoluminescence. **(b)** The optical simulations of absorption coefficient of gold nanoparticles with the size of 4 nm. **(c)** FDTD simulations, which show the field enhancement outside of the shell. The position of the core nanoparticle is shown by white dashed circle.

component, considering that Au@Ag_2Te nanoparticles did not show any distinctive excitonic peak (as shown in figure 4(a)). The close examination of the absorbance profiles of the synthesized Au@ZnTe nanocrystals from Au@Ag nanoparticles with reaction times of 30 and 50 h also showed the absorption peak located at 542 nm and 524 nm, respectively (figures 4(b) and (c)). The observed wavelength shift in the Au@ZnTe nanocrystals is possibly due to the quantum confinement effect in different ZnTe shell thicknesses.

The photoluminescence profile of the synthesized Au@ZnTe nanocrystals showed the peak positions in the range of 376–382 nm, 390–395 nm, and 404–408 nm for the nanomaterials synthesized from Au@Ag nanoparticles at the reaction times of 1, 30, and 50 h, respectively (figures 4(d)–(f)). Once the Zn cations were introduced into the system, the thermodynamically-driven cation exchange reaction occurred. By increasing the reaction time from 1 to 120 min, the Ag content decreases and ZnTe formation evolves (based on figures 3(e)–(g)) that leads to a spectrally more dominant blue emission with higher PLQY. At the same time, a small wavelength red-shift was observed by increasing the reaction time, which is possibly due to the quantum confinement effect in ZnTe shell component. The absolute PLQY of the synthesized Au@ZnTe nanocrystals with different reaction times were also measured (figures 4(g)–(i)). By increasing the reaction time from 1 min to 120 min, the PLQY showed increasing behavior. The change in the PLQY was more significant in the Au@ZnTe heterostructures synthesized from large Au@Ag nanoparticles (from 8.1% for Au@Ag_2Te to 27.2% for the Au@ZnTe with the reaction time of 120 min) in comparison with the Au@ZnTe heterostructures synthesized from small Au@Ag nanoparticles (from 2.5% for Au@Ag_2Te to 5.4% for the Au@ZnTe with the reaction time of 120 min) as shown in figures 4(g)–(i).

3. Discussion

In the hybrid metal-semiconductor nanostructures, the significantly amplified electric field in the vicinity of the plasmonic metal component can increase the optical transitions in the semiconductor [26]. Hence, the estimation of enhancement or deterioration of photoluminescent intensity is governed by the competition between relaxation, radiative, and non-radiative decay rates. In the plasmonic metal-semiconductor architectures, the metal and semiconductor are attached together. Hence, the photoluminescence intensity can be possibly quenched [27–29] or enhanced [30–32].

In order to clarify the governing factors and photoluminescent behavior in the synthesized Au@ZnTe nanostructures, we performed the plasmonic simulations by using Lumerical software [33] for core–shell structure, where gold is centered at the core with the radius of ∼4 nm and the ZnTe shell thickness was 1 nm. The Fermi energy level for gold nanoparticles and the HOMO and LUMO levels of ZnTe semiconductor were possibly positioned at −5.1 eV, −4.9 eV and −2.5 eV, respectively (figure 5(a)) [26]. The Au nanoparticles with the size of 4 nm showed absorbance peak at 543 nm based on the optical simulations (figure 5(b)). Our simulation results also showed that under the optical excitation of the Au@ZnTe nanostructures with 325 nm wavelength the field enhancement is mostly localized outside the shell and there was not any observable field enhancement inside shell (figure 5(c)). Thus, we did not observe any enhancement due to nano-antenna effect, which has a plasmonic peak of 576 nm.

Alternatively, hot-electron injection can enhance the photoluminescence. In this scenario, when photons are absorbed by Au@ZnTe, nanocrystals, electrons gain the kinetic energy, which can be calculated by using equation (1).

$$\mathrm{KE_{electron}} = \mathrm{E_{photon}} - \mathrm{E_{barrier}} - \mathrm{E_{deep-trap}}, \qquad (1)$$

where E_{photon} was the photon energy at 325 nm, E_{barrier} was considered as 2.6 eV and $E_{\mathrm{deep\text{-}trap}}$ was considered as zero. As a result, the kinetic energy of the electron ($KE_{\mathrm{electron\ at\ 325\ nm}}$) is 1.21 eV. Hence, the energy of the photons are sufficiently high to generate the hot electrons by the metallic core. Depending on the photon energy, the plasmon excitation can also non-radiatively decay into hot-carrier states on a timescale of a few femtoseconds [34–36]. There can be two probable mechanisms for photoluminescence enhancement. The first probable mechanism is that the hot electron can pass to conduction band of ZnTe shell and when it relaxes to the conduction band edge (figure 5(a)), leaves its excess energy to the lattice and results in an exciton. Finally, there will be two electrons and one hole (i.e. a negative trion). As reported theoretically [34]

and experimentally [35], radiative recombination probability is two times greater in trion structures. Second probable mechanism is generation of a biexciton. After absorption of light by surface plasmon, the kinetic energy of the hot electron leads to the generation of an exciton and a valance electron with kinetic energy, which can lead to the generation of a hole when this electron moves to the gold. In this mechanism, there will be a second hole in the valance band of the semiconductor, which consequently leads to the trion structure in the first mechanism to be converted to a biexciton. Under this probable mechanism, the radiative recombination probability can be enhanced up to 4 times [35]. In addition, the ligands of oleic acid and oleylamine will passivate the ionic traps generated by the dangling bonds. Thus, the effect of plasmonics and chemical passivation leads to a high PLQY up to 27.4%. Au@ZnTe nanocrystals, which was synthesized by other solution-based routes, showed no adverse effect on human pancreas adenocarcinoma (PL45) cell line and their fluorescence within the cells confirmed their operation *in-vitro* [37, 38]. Hence, Au@ZnTe nanocrystals with high PLQY synthesized with cation exchange hold high promise for bio-imaging.

4. Conclusions

In this study, we defined the non-epitaxial growth procedure of the Au@ZnTe nanocrystals via a step-wise organometallic synthetic route combined with the cation exchange reaction. In the first part of the synthesis procedure, Au@Ag core–shell nanoparticles were synthesized at different reaction times and the structural characterization confirmed the formation of the gold core nanoparticles with different shell thicknesses ranging from 1.0 to 3.2 monolayers. By introduction of tellurium to the reaction, an interfacial layer of Ag_2Te was formed. In the next step, the cation exchange between zinc and silver cations resulted in the crystalline zinc telluride shell formation onto the gold core. The investigation of the optical and structural properties of the synthesized Au@ZnTe core–shell nanocrystals confirmed the presence of ZnTe shell in the blue spectral region. Moreover, the synthetic optimization of Au@ZnTe nanocrystals resulted in a high PLQY level of 27%. Therefore, non-epitaxial growth holds high promise for unconventional and efficient nano-systems.

4.1. Methods and materials

4.1.1. Materials. Gold (III) chloride trihydrate ($HAuCl_4$, $\geq$ 99.9% trace metals basis), silver nitrate ($AgNO_3$, $\geq$ 99.5%), and Ethylene glycol (e.g., anhydrous, 99.8%) were purchased from Sigma-Aldrich. Poly (diallydimethylammonim chloride) solution (PDDA, M_w < 100 000, 35 wt % in water), tellurium powder (Te, 99.8% trace metals basis), oleylamine (OAM, $\geq$ 98%), oleic acid (OA, 90% technical grade), zinc chloride ($ZnCl_2$, 99.999% trace metals basis), and (TBP, $\geq$ 93.5%) were purchased from Aldrich. Deionized water was prepared with a Milli-Q water purification system. All chemicals were used without further purification.

4.1.2. Synthesis of Au@Ag nanoparticles. In order to synthesize Au@Ag nanoparticles, the previous study [24] was used with modifications. In a typical synthesis, 21.2 mg $HAuCl_4$ was mixed with 7.22 mg $AgNO_3$, 1 ml PDDA and 10 ml e.g. in a reaction flask. The reaction flask was heated at 160 °C for different reaction times in order to achieve different sizes of Au@Ag nanoparticles. As the reaction time increased from 1 h to 50 h, the color of the solution changed due to the formation of the Ag shell with different thicknesses. Three different Au@Ag core–shell structures synthesized at 1, 30 and 50 h were selected for further shelling procedure.

4.1.3. Synthesis of Au@Ag_2Te nanoparticles. Once the Au@Ag nanoparticles were synthesized, 20 mg Te powder, 5 ml OAM and 5 ml OA were added to the reaction flask and heated at 100 °C for 30 min in order to achieve the Au@Ag_2Te nanoparticles. Due to the formation of Ag_2Te, the color of the solution became dark at this stage.

4.1.4. Synthesis of Au@ZnTe nanocrystals. 20 mg $ZnCl_2$ and 50 μl TBP were added to the reaction flask containing Au@Ag_2Te nanoparticles. Then, the flask was heated at 50 °C for 30 min to complete the reaction. Aliquots were taken at different time interval in order to investigate the optical properties. After the synthesis, the reaction mixture was filtered and centrifuged at 5000 rpm for 15 min. The dark color solution was dispersed in toluene for further characterization.

4.1.5. The structural properties of the nanocrystals. The high resolution transmission electron microscopy (HRTEM) was performed using a FEI Talos F200S 200 k microscope with an accelerating voltage of 200 keV. For XRD measurements, multiple layers of nanoparticle solution were drop-casted on a glass substrate, left to dry and analyzed in a Bruker D2 Phaser x-ray diffractometer with Cu Kα radiation ($\lambda = 1.541$ Å).

4.1.6. The optical properties of the nanocrystals. The photoluminescence and UV/Visible absorbance spectra of synthesized nanocrystals were performed by Edinburgh Instruments Spectroflourometer FS5 with Xenon lamp. The nanoparticle solutions were excited with 335 nm wavelength. The integrating sphere was used to measure absolute PLQY of the synthesized nanocrystals. Standard quartz cuvettes with the cross dimensions of 1 $\times$ 1 cm^2 were used for photoluminescence, UV/Visible and PLQY measurements.

Acknowledgments

S.N. acknowledges the support by the European Research Council (ERC) under the European Union's Horizon 2020 Research and Innovation Programme (Grant agreement no. 639846). S.N. acknowledges the support by the Turkish Academy of Sciences (TÜBA-GEBİP; The Young Scientist Award Program) and the Science Academy of Turkey (BAGEP; The Young Scientist Award Program).

Conflicts of interest

The authors declare no competing financial interests.

ORCID iDs

Sadra Sadeghi https://orcid.org/0000-0002-8569-1626
Rustamzhon Melikov https://orcid.org/0000-0003-2214-7604

References

[1] Zhong C-J and Maye M M 2001 Core–shell assembled nanoparticles as catalysts *Adv. Mater.* **13** 1507–11
[2] Caruso F 2001 Nanoengineering of particle surfaces *Adv. Mater.* **13** 11–22
[3] Bahmani Jalali H, Mohammadi Aria M, Dikbas U M, Sadeghi S, Ganesh Kumar B, Sahin M, Kavakli I H, Ow-Yang C W and Nizamoglu S 2018 Effective neural photostimulation using indium-based type-II quantum dots *ACS Nano* **12** 8104–14
[4] Sadeghi S, Mutcu S E, Srivastava S B, Aydindogan G, Caynak S, Karslı K, Melikov R and Nizamoglu S 2018 High quality quantum dots polymeric films as color converters for smart phone display technology *Mater. Res. Express* **6** 035015
[5] Karatum O, Jalali H B, Sadeghi S, Melikov R, Srivastava S B and Nizamoglu S 2019 Light-emitting devices based on type-II InP/ZnO quantum dots *ACS Photonics* **6** 939–46
[6] Bahmani Jalali H, Sadeghi S, Sahin M, Ozturk H, Ow-Yang C W and Nizamoglu S 2019 Colloidal aluminum antimonide quantum dots *Chem. Mater.* **31** 4743–7
[7] Sadeghi S, Abkenar S K, Ow-Yang C W and Nizamoglu S 2019 Efficient white LEDs using liquid-state magic-sized CdSe quantum dots *Sci. Rep.* **9** 10061
[8] Zhang J, Tang Y, Weng L and Ouyang M 2009 Versatile strategy for precisely tailored core@ shell nanostructures with single shell layer accuracy: the case of metallic shell *Nano Lett.* **9** 4061–5
[9] Zhou Y, Zhao H, Ma D and Rosei F 2018 Harnessing the properties of colloidal quantum dots in luminescent solar concentrators *Chem. Soc. Rev.* **47** 5866–5890
[10] Pietryga J M, Werder D J, Williams D J, Casson J L, Schaller R D, Klimov V I and Hollingsworth J A 2008 Utilizing the lability of lead selenide to produce heterostructured nanocrystals with bright, stable infrared emission *J. Am. Chem. Soc.* **130** 4879–85
[11] Son D H, Hughes S M, Yin Y and Alivisatos A P 2004 Cation exchange reactions in ionic nanocrystals *Science* **306** 1009–12
[12] Zhang J, Tang Y, Lee K and Ouyang M 2010 Nonepitaxial growth of hybrid core-shell nanostructures with large lattice mismatches *Science* **327** 1634–8
[13] Abel K A, Qiao H, Young J F and van Veggel F C 2010 Four-fold enhancement of the activation energy for nonradiative decay of excitons in PbSe/CdSe core/shell versus PbSe colloidal quantum dots *J. Phys. Chem. Lett.* **1** 2334–8
[14] Zhao H, Liang H, Vidal F, Rosei F, Vomiero A and Ma D 2014 Size dependence of temperature-related optical properties of PbS and PbS/CdS core/shell quantum dots *J. Phys. Chem.* C **118** 20585–93
[15] Meinardi F, McDaniel H, Carulli F, Colombo A, Velizhanin K A, Makarov N S, Simonutti R, Klimov V I and Brovelli S 2015 Highly efficient large-area colourless luminescent solar concentrators using heavy-metal-free colloidal quantum dots *Nat. Nanotechnol.* **10** 878–85
[16] Wang Z 2000 Transmission electron microscopy of shape-controlled nanocrystals and their assemblies *J. Phys. Chem.* B **6** 1153–1175
[17] Huang J, Wang X, Hogan N L, Wu S, Lu P, Fan Z, Dai Y, Zeng B, Starko-Bowes R and Jian J 2018 Nanoscale artificial plasmonic lattice in self-assembled vertically aligned nitride–metal hybrid metamaterials *Adv. Sci.* **5** 1800416
[18] Jang E-P, Han C-Y, Lim S-W, Jo J-H, Jo D-Y, Lee S-H, Yoon S-Y and Yang H 2019 Synthesis of alloyed ZnSeTe quantum dots as bright, color-pure blue emitters *ACS Appl. Mater. Interfaces* **11** 46062–9
[19] Peng X, Schlamp M C, Kadavanich A V and Alivisatos A P 1997 Epitaxial growth of highly luminescent CdSe/CdS core/shell nanocrystals with photostability and electronic accessibility *J. Am. Chem. Soc.* **119** 7019–29
[20] McBride J, Treadway J, Feldman L C, Pennycook S J and Rosenthal S J 2006 Structural basis for near unity quantum yield core/shell nanostructures *Nano Lett.* **6** 1496–501
[21] Pearson R G 1963 Hard and soft acids and bases *J. Am. Chem. Soc.* **85** 3533–9
[22] Malathi S, Ezhilarasu T, Abiraman T and Balasubramanian S 2014 One pot green synthesis of Ag, Au and Au–Ag alloy nanoparticles using isonicotinic acid hydrazide and starch *Carbohydr. Polym.* **111** 734–43
[23] Biasotto G, Chiadò A, Novara C, Fontana M, Armandi M, Zaghete M A, Giorgis F and Rivolo P 2020 Graphenic aerogels decorated with Ag nanoparticles as 3D SERS substrates for biosensing *Part. Part. Syst. Charact.* **37** 2000095
[24] Li C, Sun L, Sun Y and Teranishi T 2013 One-pot controllable synthesis of Au@ Ag heterogeneous nanorods with highly tunable plasmonic absorption *Chem. Mater.* **25** 2580–90
[25] Mahmood W, Awan S U, Ud Din A, Ali J, Nasir M F, Ali N, Kamran M, Parveen B, Rafiq M and Abbas Shah N 2019 Pronounced impact of p-type carriers and reduction of bandgap in semiconducting ZnTe thin films by Cu doping for intermediate buffer layer in heterojunction solar cells *Materials* **12** 1359
[26] Jiang R, Li B, Fang C and Wang J 2014 Metal/semiconductor hybrid nanostructures for plasmon-enhanced applications *Adv. Mater.* **26** 5274–309
[27] Mokari T, Rothenberg E, Popov I, Costi R and Banin U 2004 Selective growth of metal tips onto semiconductor quantum rods and tetrapods *Science* **304** 1787–90
[28] Chen W-T, Yang -T-T and Hsu Y-J 2008 Au-CdS core− shell nanocrystals with controllable shell thickness and photoinduced charge separation property *Chem. Mater.* **20** 7204–6
[29] Chen W-T and Hsu Y-J 2010 L-cysteine-assisted growth of core− satellite ZnS− Au nanoassemblies with high photocatalytic efficiency *Langmuir* **26** 5918–25
[30] Bian J-C, Yang F, Li Z, Zeng J-L, Zhang X-W, Chen Z-D, Tan J Z Y, Peng R-Q, He H-Y and Wang J 2012 Mechanisms in photoluminescence enhancement of ZnO nanorod arrays by the localized surface plasmons of Ag nanoparticles *Appl. Surf. Sci.* **258** 8548–51
[31] Mahanti M and Basak D 2012 Highly enhanced UV emission due to surface plasmon resonance in Ag–ZnO nanorods *Chem. Phys. Lett.* **542** 110–6
[32] Shanmugapriya T and Ramamurthy P 2013 Photoluminescence enhancement of nanogold decorated CdS quantum dots *J. Phys. Chem.* C **117** 12272–8
[33] Melikov R, Srivastava S B, Karatum O, Dogru I B, Jalali H B, Sadeghi S, Dikbas U M, Ulgut B, Kavakli I H and Nizamoglu S 2020 Plasmon-coupled photocapacitor

neuromodulators *ACS Appl. Mater. Interfaces* **12** 35940
[34] Sahin M and Koç F 2013 A model for the recombination and radiative lifetime of trions and biexcitons in spherically shaped semiconductor nanocrystals *Appl. Phys. Lett.* **102** 183103
[35] Cihan A F, Hernandez Martinez P L, Kelestemur Y, Mutlugun E and Demir H V 2013 Observation of biexcitons in nanocrystal solids in the presence of photocharging *ACS Nano* **7** 4799–809
[36] Jia C, Li X, Xin N, Gong Y, Guan J, Meng L, Meng S and Guo X 2016 Interface-engineered plasmonics in metal/semiconductor Heterostructures *Adv. Energy Mater.* **6** 1600431
[37] Dunpall R, Lewis E A, Haigh S J, O'Brien P and Revaprasadu N 2015 Synthesis of biocompatible Au–ZnTe core–shell nanoparticles *J. Mater. Chem.* B **3** 2826–33
[38] Dunpall R and Revaprasadu N 2016 An in vitro and in vivo bio-interaction responses and biosafety evaluation of novel Au–ZnTe core–shell nanoparticles *Toxicol. Res.* **5** 1078–89